Revisiting the tropical Atlantic western boundary circulation from a 25-year time series of satellite altimetry data

Djoirka M. Dimoune[1,4], Florence Birol[2], Fabrice Hernandez[1,2], Fabien Léger[2], Moacyr Araujo[1,3]

[1]Laboratorio de Oceanografia Física Estuarina e Costeira (LOFEC), Departamento de Oceanografia da Universidade Federal de Pernambuco (UFPE), Cidade Universitária, Avenida Arquitetura s/n, 50740-550 Recife, PE, Brazil
[2]LEGOS, Université de Toulouse, CNES, CNRS, IRD, 14 avenue Edouard Belin, 31400, France
[3]Brazilian Research Network on Global Climate Change (Rede CLIMA), Av. dos Astronautas, 1758, 01227-010 São José dos Campos, SP, Brazil
[4]Nansen Tutu Center for Marine Environmental Research, Dept of Oceanography, University of Cape Town, Rondebosch, Cape Town, 7700, South Africa

Correspondance to: Djoirka M. Dimoune (pmintodimoune@gmail.com)

Abstract. Geostrophic currents derived from altimetry are used to investigate the surface circulation in the Western Tropical Atlantic over the 1993-2017 period. Using six horizontal sections defined to capture the current branches of the study area, we investigate their respective variations at both seasonal and interannual time-scales as well as the spatial distribution of these variations in order to highlight the singularities of the currents on their route. Our results show that the central branch of the South Equatorial Current, its northern branch near the Brazilian coast, the North Brazil Current component located south of the equator and the Guyana Current have similar annual cycles, with maxima/minima respectively, during late boreal winter/boreal fall when the Intertropical Convergence Zone is at its southernmost/northern location. In contrast, the seasonal cycles of the North Brazil Current branch located between the equator and 7-8° N, its retroflected branch, the northern branch of the South Equatorial Current to the west of 35° W and the North Equatorial Countercurrent show maxima/minima during late boreal summer/boreal spring following the remote wind stress curl strength variation. West of 32° W, an eastward current is observed between 0°-2° N, identified as the equatorial extension of the retroflected branch of the North Brazil Current. It is part of a large cyclonic circulation observed between 0°-6° N and 35°-45° W during boreal spring. We also observed a secondary North Brazil Current retroflection flow during the second half of the year which leads to the two-core structure of the North Equatorial Countercurrent, and might be related to the wind stress curl seasonal changes. Eastward, the North Equatorial Countercurrent weakens and its two-core structure is underdeveloped due to the weakening of the wind stress. At interannual scales, depending on which side of the equator, the North Brazil Current exhibits two opposite

36 scenarios related to the tropical Atlantic Meridional Mode phases. The interannual variability

37 of the North Equatorial Countercurrent and of the northern branch of the South Equatorial

38 Current (in terms of both strength and/or latitudinal shift) at 42° W are also associated to the

39 Atlantic Meridional Mode. However, they are associated to the Atlantic mode phases at 32° W.

40

41 1   Introduction

42 The energetic Western Tropical Atlantic (WTA) boundary surface circulation is known to play

43 a key role in the transport of heat, salt and water mass from the southern to the northern

44 hemispheres of the Atlantic Ocean. It corresponds to a superposition of the return branch of the

45 thermohaline Atlantic Meridional Overturning Circulation (AMOC), the flow from the

46 Subtropical Cells and Sverdrup dynamics (Schmitz and McCartney, 1993; Schott et al., 2004,

47 2005; Rodrigues et al., 2007, Tuchen et al., 2019, 2020). The region is also known to be

48 influenced by large mesoscale activities due to the barotropic instabilities of the currents. The

49 most dominant mesoscale structures are the large rings generated by North Brazilian Current

50 (NBC) retroflection (Aguedjou et al., 2019; Aroucha et al., 2020). A regional scheme of the

51 surface currents in the study area is proposed in Fig. 1. It is derived from a global analysis of

52 the different studies mentioned hereafter.

53 From 5° S to 15° N, the surface boundary circulation is formed by the NBC flowing northward

54 along the South American shelf. It carries tropical waters originating from the South Atlantic

55 subtropical gyre and contributes to interhemispheric water transport (Johns et al., 1990; 1998;

56 Peterson and Stramma, 1991; Stramma and England, 1999; Fratantoni et al., 2000; Silva et al.,

57 2009; Zheng and Giese, 2009; Garzoli and Matano, 2011). The NBC has its origin near 5° S,

58 with two sources: the central branch of the westward South Equatorial Current (cSEC); and the

59 along-shelf equatorward North Brazil Undercurrent (NBUC) which surfaces around 5-6° S

60 (Schott et al., 1998, Dossa et al., 2020). The latter advects warm waters from the South

61 Equatorial Current (SEC) through its southern branch (Schott et al., 1995). Further north,

62 around 5° N, the NBC is also fed by the northern branch of the SEC (nSEC) (Goes et al., 2005).

63 Then, between 5°-9° N and 45-50° W, a large part of the NBC retroflects to form a

64 southeastward retroflected branch (called hereinafter rNBC). Between 3° N and 8° N, this

65 branch first feeds the eastward North Equatorial Countercurrent (NECC) throughout the year,

66 except during the boreal spring. At that time, the NECC is fed only by the North Equatorial

67 Current (NEC) (Bourlès et al., 1999a; Goes et al., 2005). The NECC flows eastward between

68 2° N and 12° N, and crosses the tropical Atlantic (Didden and Schott, 1992; Ffield, 2005;

69 Urbano et al., 2008; Araujo et al., 2017). During the second half of the year, this current shows

70 two cores that can separate into a southern and a northern branch (called sNECC and nNECC,

71 respectively: Urbano et al., 2006; 2008).

72 At depth, around 3-8° N, Cochrane et al. (1979) and Schott et al. (2004) suggested that, part of

73 the rNBC also feeds the eastward North Equatorial UnderCurrent (NEUC) located around 5°

74 N. In addition, between 2° S and 3° N, the rNBC feeds the subsurface eastward Equatorial

75 UnderCurrent (EUC) (Hisard and Hénin, 1987; Bourlès et al., 1999b; Hazeleger et al., 2003;

76 Hazeleger et de Vries, 2003; Schott et al., 1995; 2004). North of 10° N, the part of the NBC

77 which has not retroflected flows northwestward along the Guyana coast, forming the Guyana

78 Current. The latter is also fed seasonally by the NEC (Johns et al., 1998) and transports warm

79 equatorial waters into the Caribbean Sea (Stramma and Schott, 1999; Garzoli et al., 2003).

80 The WTA boundary surface circulation is wind-driven. In the vorticity equation, the terms that

81 dominate localy are the Ekman pumping and the divergence of the geostrophic currents (Garzoli

82 and Katz, 1983; Urbano et al., 2006). Previous studies of Garzoli and Katz (1983), Jochum and

83 Malanotte-Rizzoli (2003) and Verdy and Jochum (2005) about the WTA boundary circulation

84 and the NECC indicate that, west of 32° W, the Sverdrup balance is no longer satisfied; the

85 advection terms of the relative vorticity due to the eddies and the mean flow become then

86 important. North of the equator, the region is characterized by strong seasonal variability of the

87 wind. The Trade Winds variations influence the current system formed by the NBC, the NBC

88 retroflection (NBCR), the rNBC and the NECC. In particular the NBCR location, the NBC

89 transport and the NECC position/transport respond to the seasonal changes in the wind regimes

90 (Johns et al., 1990; 1998; Garzoli et al., 2003; 2004; Urbano et al., 2006; 2008). This wind

91 influence is traduced by latitudinal shifts of the currents, in conjunction with the Intertropical

92 Convergence Zone (ITCZ) location. The variability of the current strength appears as a regional

93 response to the wind stress curl (WSC) distribution and of the WSC strength over the basin

94 (Johns et al., 1998; Fonseca et al., 2004; Garzoli et al., 2004, Urbano et al., 2006; 2008). In the

95 equatorial region, the EUC seasonal variability depends first on the basin scale zonal pressure

96 gradient, and also to the seasonal cycle of the local wind forcing (Hisard and Hénin, 1987;

97 Provost et al., 2004; Brandt et al., 2006; Hormann and Brandt, 2007; Brandt et al., 2016).

98 The interannual variability of the WTA boundary currents has been understudied because of

99 the lack of long-term data in this area. Nevertheless, Fonseca et al. (2004), using a combination

100 of altimetry and hydrographic data from 1993 to 2000, investigated the influence of the wind

101 on both the NBCR and the NECC variability. They did not find any direct relationship between

102 them. Hormann et al. (2012), used the surface velocity data derived from drifters between 1993

103 and 2009 and highlighted a relationship between the NECC intensity/location and the tropical

104 Atlantic climate modes (ACM), represented by positive and negative phases of the Atlantic

105 zonal mode (AZM) and the Atlantic meridional mode (AMM) (Cabos et al., 2019). They found

106 the intensity to be related to the cold phase of AZM and the core location to be related to the

107 warm phase of AMM. In the equatorial Atlantic, Hormann and Brandt (2007) also found such

108 relationship, using a high-resolution ocean general circulation model, observations and sea

109 surface temperature (SST) data. They showed that the EUC transport is affected by the cold and

110 warm events of the AZM (the so called "Atlantic Niño / Niña") and confirmed the previous

111 findings of Goes and Wainer (2003) concerning the link between the interannual variability of

112 the wind and the ACM impacting the strength of the tropical Atlantic circulation.

113 In this study, we propose to revisit the scheme of the WTA boundary surface circulation using

114 a 25-year time series of gridded altimeter-derived geostrophic currents. This dataset is longer

115 than the one used by Fonseca et al. (2004) and allows us to provide a more robust description

116 of the current branches described above, as well as of their seasonal and interannual variations.

117 The data also allows us to infer regional relationship among these currents. The paper is

118 organized as follows: in Sect. 2, the data and methods used are presented. Section 3 brings some

119 general characteristics of the current variability in the study area. In the fourth section we

120 analyze and discuss the seasonal and spatial variabilities of the surface geostrophic currents and

121 propose an updated seasonal map of the WTA surface circulation. The interannual variability

122 of the circulation is analyzed in Sect. 5. Section 6 is devoted to a general discussion, and Sect.

123 7 offers a summary and some perspectives.

124

125

126
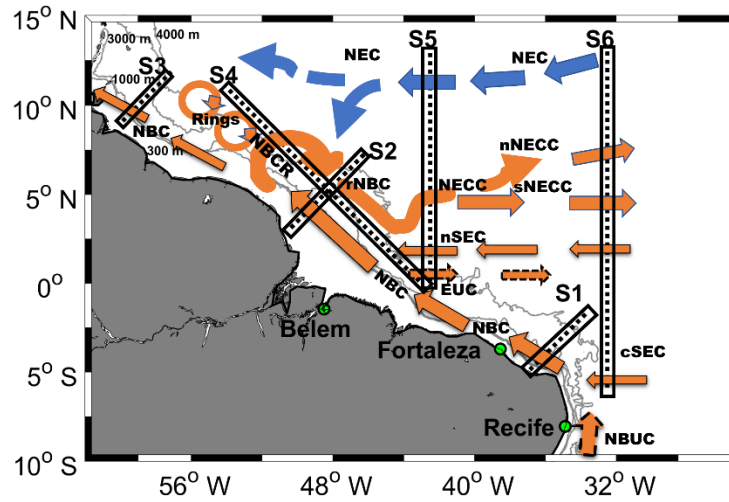
Figure 1. Schematic view of the western boundary surface circulation in the tropical Atlantic based on Schott et al. (2004), Goës et al. (2005), Urbano et al. (2006; 2008) and Aroucha et al. (2019). The distribution of the horizontal section used to study the different current branches are also indicated in black: S1, S2, S3, S4, S5 and S6. Solid and dashed arrows are the upper and the subsurface currents, respectively. The blue and orange colors of the arrows show connections with the northern and southern hemisphere waters, respectively. Acronyms are listed in Table 1. The 300 m, 1000 m, 3000 m and 4000 m isobaths (grey lines) are from the ETOPO2v1 database.

2   Data and methods

2.1   Altimeter-derived geostrophic currents

From along-track altimetry sea surface height measurements of all available satellite missions, the Copernicus Marine Environment Monitoring Service (CMEMS) produces daily maps of ocean dynamic topography, and derives then geostrophic surface currents. Here, we use the SEALEVEL_GLO_PHY_L4_REP_OBSERVATIONS_008_047 product (https://resources.marine.copernicus.eu) from January 1993 to December 2017. Daily maps of dynamic topography are estimated by optimal interpolation on $0.25° \times 0.25°$ global grid (details can be found in Pujol et al., 2016), and the geostrophic currents are computed using the 9-points stencil width methodology (Arbic et al., 2012) for latitudes outside the equatorial band (Equator $\pm 5°$) and in the equatorial band, the currents have been calculated using the Lagerloef methodology (Lagerloef et al., 1999) which used a β-plane approximation due to the fact that the Coriolis parameter is vanishing.

To validate geostrophic current estimates in the equatorial region, we have compared them to the PIRATA current meter mooring data available in the study area (0°N, 35°W) over the 11/10/2017-29/01/2018 (Fig. 1 in the supplementary material). The data of the current meter were obtained at 12-m depth and have been averaged each 5 days. The results of the comparison with the geostrophic currents interpolated to the same location were satisfactory. A correlation

of 0.71 is found on their zonal components while the one on the meridional components is lower (Figure 1a-b in the supplementary material). The mean biases/standard deviation differences for both components are respectively, 0.04/0.11 m s^{-1} and 0.14/0.03 m s^{-1}. The similar values were also found by Lagerloef et al. (1999) in the western equatorial Pacific when comparing the geostrophic currents to the current meter mooring data at 10-m depth. These results give credit to the geostrophic estimates used in this work for the equatorial region. However, as reported earlier, their values are underestimated compared to other observations (Picaut et al., 1989; Lagerloef et al., 1999, Pujol et al., 2016). The PIRATA 0-35°W current meter was also able to capture an eastward flow at this location from November 2018 to March 2019. This confirms the previous findings of the Bourlès et al. (2019) and legitimizes our desire to know more about this flow.

Table 1. Acronyms and abbreviations

AMM	Atlantic Meridional Mode
AMOC	Atlantic Meridional Overturning Circulation
AZM	Atlantic Zonal Mode
EUC	Equatorial Undercurrent
ITCZ	Intertropical Convergence Zone
NBC	North Brazil Current
rNBC	Retroflected branch of the NBC
NBCR	North Brazil Current Retroflection
nNBCR	Northern NBCR flow
nNBCR lat	Latitude of the nNBCR maximum intensity
sNBCR	Southern NBCR flow
sNBCR lat	Latitude of the sNBCR maximum intensity
NECC	North Equatorial Countercurrent
nNECC	Northern branch of the NECC
nNECC lat	Latitude of the nNECC core
sNECC	Southern branch of the NECC
sNECC lat	Latitude of the sNECC core
PIRATA	Prediction and Research Moored Array in the Tropical Atlantic
SEC	South Equatorial Current
cSEC	Central branch ot the SEC
nSEC	Northern branch of the SEC
VnNBCR	Value of the nNBCR maximum speed
VsNBCR	Value of the sNBCR maximum speed
VnNECC	Value of the nNECC core speed
VsNECC	Value of the sNECC core speed
X	Equatorial Surface Eastward flow
WSC	Wind Stress Curl
WSC neg max	Maximum negative WSC
WSC strength	WSC strength
WTA	Western tropical Atlantic

For the present work, focusing on the seasonal and interannual variability, the daily gridded velocity fields from CMEMS have been averaged monthly. Note that, data with high variability (standard deviation > 0.4) have been removed. They are found in the Amazon region which is not a primary area of interest for this study, and where, the annual mean current speeds are unrealistic (higher than 2.5 m s^{-1}), probably due to geographically correlated errors (Pujol et al., 2016). We have then defined six horizontal sections (called S1, S2, S3, S4, S5 and S6, respectively), so that they cross perpendicularly at least one of the regional current branches (see Fig. 1). For each section, the original zonal and meridional surface velocity components have been rotated in order to derive the along-section and cross-section velocity components. In this study, we considered only the cross-section component, and the rotation angles considered for the oblique sections S1-S2-S3/S4 are 45°/315°.

2.2 Wind velocity

Monthly wind velocity fields from the ERA5 atmospheric reanalysis produced by the European Centre for Medium-Range Weather Forecasts (ECMWF, http://www.ecmwf.int) are used in order to evaluate the influence of the remote winds on the WTA ocean circulation. They were downloaded from the Copernicus Climate Change data server over the January 1993 - December 2017 period. We used the wind velocity data to calculate the wind stress field as follows.

The zonal and meridional components of the wind stress, ζ_x and ζ_y are calculated using empirical formulations (Large and Pond; 1981: Gill, 1982; Trenberth et al., 1990) following NRSC (2013):

$$\tau_x = \rho_{air} C_D W^* U \tag{1}$$

$$\tau_y = \rho_{air} C_D W^* V \tag{2}$$

where U/V represent the zonal/meridional wind velocity components; W, the wind speed amplitude; ρ_{air}, the air density (1.2 kg m^{-2}); C_D, the drag coefficient at the ocean surface, calculated according to Large and Pond (1981).

The wind stress curl (WSC) is then deduced following Gill (1982):

$$Curl(\tau) = \frac{\partial \tau_y}{\partial x} - \frac{\partial \tau_x}{\partial y} \tag{3}$$

194 Over the tropical Atlantic, from the WSC near-zero values, the ITCZ locations have been

195 determined. Then, the minimum/maximum of the negative/positive WSC values has been

196 found, and the WSC strength values (sum of the absolute minimum negative and maximum

197 positive values) have been computed. Each of these parameters is zonally averaged over the

198 region covering 6° S -16° N, and 30° W-0° E, following Fonseca et al. (2004).

2.3   Sea Surface temperature

200 Monthly estimates of Sea Surface temperature (SST) are also used in order to compute the

201 Atlantic climate mode indexes and evaluate their possible relationship with the interannual

202 changes observed in the WTA boundary circulation. A global gridded SST product, with a 1°

203 spatial resolution is downloaded from the NOAA repository

204 (https://www.esrl.noaa.gov/psd/data/gridded/data.noaa.oisst.v2.html, Reynolds et al. 2002).

205 The AZM index is calculated considering the SST anomalies (SSTA) relative to the 1993-2017

206 monthly climatology in the ATL3 region bounded by 3° S-3° N/20° W-0° E (Zebiak, 1993,

207 Hormann et al., 2012). The AMM index is also based on SSTA relative to the 1993-2017

208 monthly climatology, and calculated as the difference between the spatial average SSTA in the

209 box 5° N-25° N/60° W-20° W and the spatial average SSTA in the box 20° S-5° N/30° W-10°

210 E (Servain, 1991; Hormann et al., 2012).

3   General characteristics of the circulation in the Western Tropical Atlantic

212 The mean WTA surface geostrophic circulation is first derived by averaging the gridded

213 altimetry current maps over 1993-2017 (Fig. 2a). We distinguish three different areas. From

214 south/east to north/west:

1) The NBC formation area starting around 5°S: the westward cSEC flowing north of 6°S (mean value of ~ 0.3 m s^{-1}) feeds the NBC-NBUC current system around 34°-36° W. The NBC amplitude increases along its northward along-shelf course, up to 0.8 m s^{-1} around 3° S. Then it slows down toward the equator, before increasing again north of 3° N. Along the coast, farther north, its mean velocities are again weaker, with values of ~ 0.3 m s^{-1}.

2) The NBC retroflection region between 5°-8° N: in this area, the NBC undergoes an eastward recirculation, which feeds a southeastward path of current so-called the NBC retroflected branch (rNBC). The rNBC reaches annual mean velocities of ~0.6 m s^{-1}.

224   3) The area located between 3°-6° N and 42°-46° W: it represents the region where the
225   rNBC meanders with an annual mean velocity of 0.5 m s^{-1} to partly feed the surface
226   eastward NECC which decays along its course. This area is located in the region of high
227   wind variability (Figure not shown).

228 In addition, we also observe the westward nSEC flowing between 2°-6° N, with stronger
229 velocity values at the eastern part of the basin (mean velocity larger than 0.3 m s^{-1}).

230 We computed the mean power spectral density of the daily geostrophic current time series in
231 order to detect the dominant components of the WTA current variations (not shown). It
232 highlighted three main energy zones:

233   1) at intraseasonal scales with different peaks at periods less than 120 days,

234   2) at seasonal scale,

235   3) at interannual timescale, with peaks at periods larger than 600 days.

236 We filtered the velocity time series using different cutoff frequencies in order to isolate each of
237 this component of the current variability: below 120 days, between 120 days and 600 days and
238 above 600 days. Then, we computed the ratio between the standard deviation of each filtered
239 current field and of the total current field. The resulting maps (Fig. 2b-d) show the relative
240 importance of each component with regard to the total variance, as a function of the location.
241 We observe the predominance of the seasonal variability in the whole WTA (overall ratio of
242 0.44), with the highest values (0.48) observed along the continental shelf, in the NBC region,
243 and between 0°-2° S east of 36° W. Intraseasonal fluctuations are also important in the same
244 areas (with largest ratio of 0.44) while the interannual variability is weaker and the highest
245 values (>0.2) are found in the NECC area north/east of 4° N/40° W (consistent with Richardson
246 and Walsh, 1986). In this study, we focus on the seasonal and interannual timescales.

247
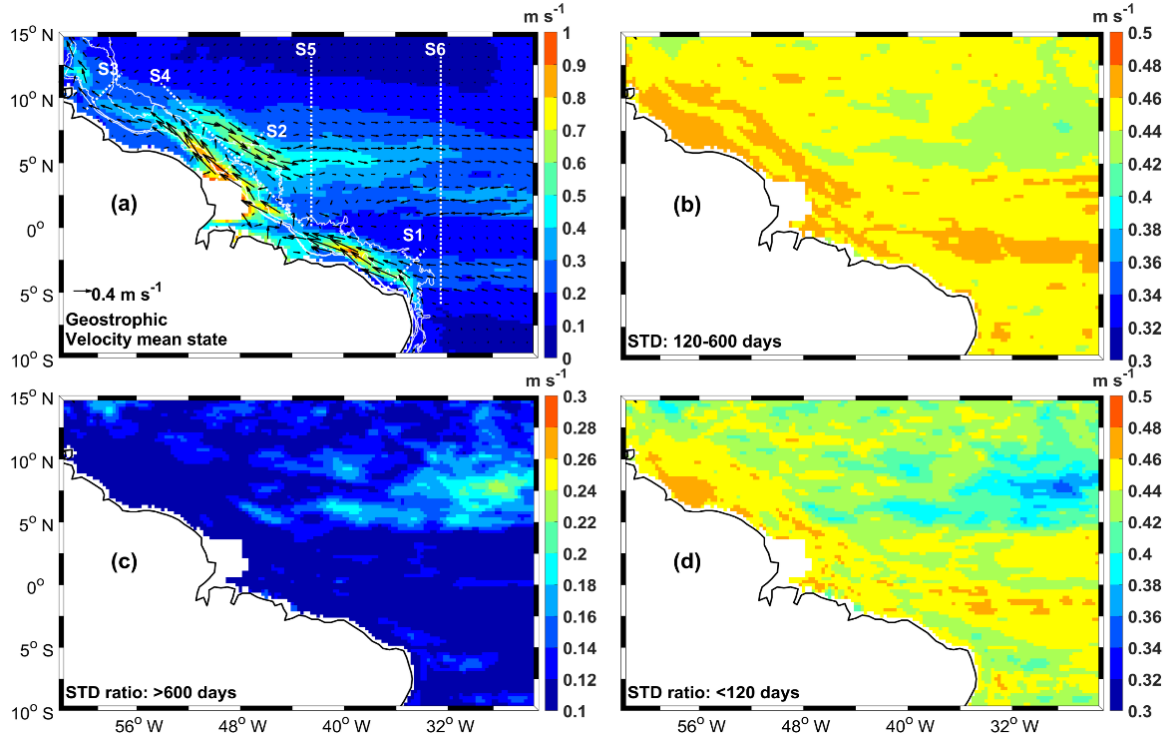
Figure 2. (a) Temporal mean of the geostrophic currents (amplitude in m s^{-1} and vectors) in the study area between 1993 to 2017; **(b), (c)** and **(d)** ratios between the standard deviations of the currents for the signals between 120 and 600 days, longer than 600 days and shorter than 120 days, respectively, and the standard deviation of the total currents. The white dashed lines S1, S2, S3, S4, S5, S6 in **(a)** represent the cross-sections of the currents, and the solid white lines are the 300 m, 1000 m, 3000 m and 4000 m isobaths. Note that, the colobar of **(c)** is different than the ones of (b) and (d).

Then we monthly averaged the daily geostrophic currents and extracted the cross-section geostrophic velocities along the six sections defined above (Fig. 1). In order to remove the intraseasonal variability, the monthly velocity estimates are further low-pass filtered using a 4-month cutoff frequency. The time-space diagrams (also called Hovmöller diagrams) along the six sections are plotted in Fig. 3. We can clearly observe large changes in both time and space with respect to the different current branches, illustrating the complexity of the surface circulation in the WTA. The seasonal and, in a lesser extent, the interannual current fluctuations mentioned above are clearly visible in the different sections. For each of them, the time-average current values are also computed as a function of the latitude (left-side plots in Fig. 3), highlighting the mean spatial extension of the current paths crossing the corresponding section. Note that in addition to the main currents mentioned in Fig. 1, between 2° S-2° N, the sections 4 to 6 show an eastward surface current, located at the same location where the EUC flows, west of 44°W in the subsurface along the equator (Schott et al., 1998). Depending on the season

269 the EUC core is known to be located between about 100-m depth and 50-m depth when it

270 surfaces to reach the near-surface (Brandt et al., 2016). At 44° W, Bourlès et al. (1999b) have

271 also noticed the presence of an eastward surface flow above the EUC, which was identified to

272 be different than the EUC. So, we chose to name it X hereinafter in order to further investigate

273 this signal and its origin.

274 Table 2 summarizes the mean current width derived along the different sections (using left-side

275 plots in Fig. 3). Note first that a positive current convention is chosen for the sections as follows:

276 northward NBC along sections 1 to 3; eastward NBCR along section 4; eastward NECC along

277 sections 5 and 6, and eastward X flows along sections 4 to 6. Hence, the signatures of the rNBC

278 on the section 2, the nSEC (sections 4 to 6) and the cSEC (section 6) are considered as negative.

279 From Table 2, we observe that the NBC becomes narrower from the section 1 to the section 2.

280 The retroflection zone (section S4, Fig. 3S4) extends from 3.7° N to 10.5° N, in agreement with

281 Fonseca et al., (2004) who found the northernmost position of the NBCR around 11° N. North

282 of the retroflection, the NBC along the Guyana coast is weaker, but broader relatively to the

283 section 2 (NBC2 and NBC3 in Fig. 3). From section 6 to 4, the nSEC signature changes. It is

284 wider at 32° W (nSEC6), then narrower at 42° W (nSEC5), and widens again closer to the shelf

285 at 44° W (nSEC4) (respectively 550, 67 and 190 km in Table 2). The NECC extension also

286 varies from 32° W to 42° W, and is wider and located further north on the east, with a mean

287 width extending from 860 km (NECC5) to 920 km (NECC6).

288 **Table 2.** Extension in latitude and km of the different currents branches crossing the different sections: NBC1,

289 NBC2 and NBC3 are respectively the North Brazil Current captured on sections 1, 2 and 3; NECC5 and NECC6

290 are respectively the North Equatorial Countercurrent on the sections 5 and 6; nSEC4, nSEC5 and nSEC6 are

291 respectively the northern branch of the South Equatorial Current (SEC) on the sections 4, 5 and 6; cSEC6 is the

292 central branch of the SEC on the section 6; and X4, X5 and X6 are the equatorial eastward flow X on respectively

293 on the sections 4, 5 and 6.

List of current paths	Latitudinal coverage	Current width (km)
NBC1	1.3° S-4.6° S	~ 520
NBC2	3.6° N-5° N	~ 220
rNBC2	5° N-7.4° N	~ 380
NBC3	9.1° N-11.9° N	~ 440
NBCR4	3.7° N-10.5° N	~ 760
nSEC4	2° N-3.7° N	~ 190
X4	1.2° N-2° N	~ 120
NECC5	2.4° N-10.1° N	~ 860
nSEC5	1.7° N-2.3° N	~ 70
X5	0° N-1.7° N	~ 190
NECC6	4.1° N-12.4° N	~ 920
nSEC6	0° N-4.1° N	~ 550
X6	0° S-1.4° S	~ 110
cSEC6	1.4° S-5.9° S	~ 500
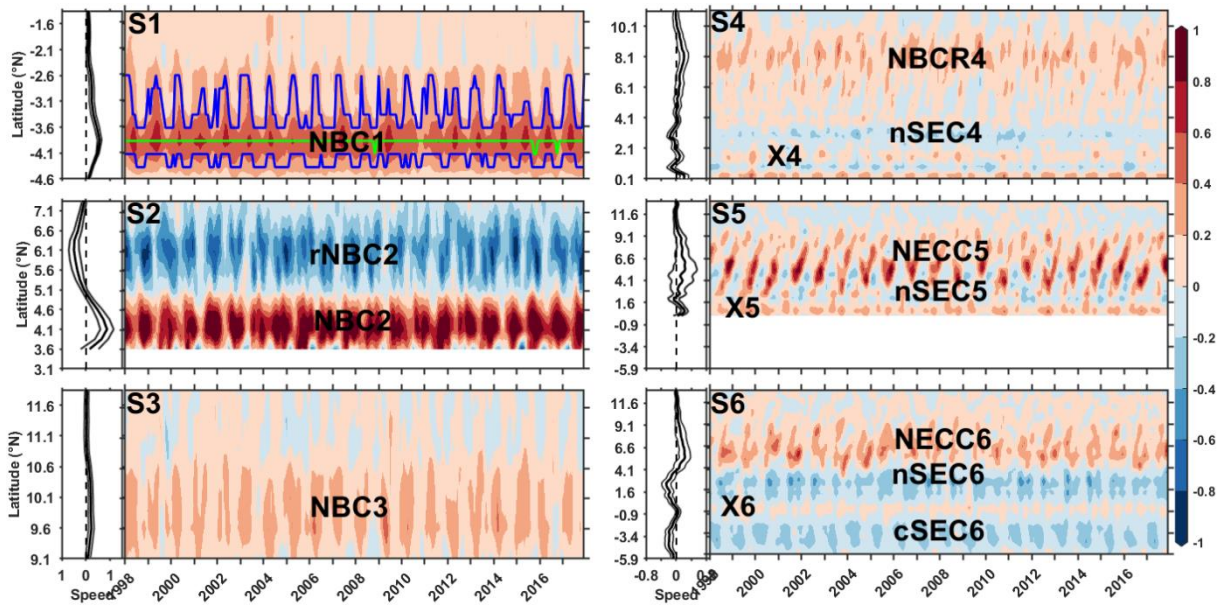
294

295

Figure 3. Hovmöller diagrams (1993 to 2017) of the cross-section current components (m s^{-1}) for S1, S2, S3 S4 S5 and S6. At the left of each diagram, the time series of time averages of the cross-section current (thick lines), framed by their corresponding standard deviations (thin lines) are plotted as a function of latitude. The red (blue) colors show the northward/eastward (southward/westward) directions of the cross-currents. Acronyms are listed in Table 1. The numbers next to the acronyms represents the number of the section. The green line in S1 indicates the time series of the maximum velocity of the cross-section current (NBC), and is framed by the time series of the maximum velocities divided by 2 (blue lines) over 1993-2017 period.

303

In order to further investigate the temporal variations of the current amplitude or strength, the maximum speed values of each current paths have been determined for each month. These maxima correspond to the current core and are called Vmax hereafter: (see Fig. 3, green line on S1), and their location corresponds to the location of the current core. Then, to estimate the current relative strength/intensity, we have considered the part of the sections of velocities larger than Vmax/2 (see Fig. 3, blue lines on S1), and we finally computed the strength/intensity values by averaging the velocity values of these parts over time. The width of the currents (Table 2) is determined by the mean of the current over the whole period of study (1993-2017) at each grid point (see left boxes of the Hovmöller diagrams of Fig. 3). Then, knowing the sign or direction of the current (eastward or westward), the corresponding time series are used to define the width by finding the limits where the current is null. Note that the current strength/intensity has also been computed by averaging velocity values over the entire width of the current paths (e.g., not only where the velocity is larger than Vmax/2), but the results did not correctly reflect the current variability observed in Fig. 3 and Fig. 4 (not shown).

For the NBCR and the NECC, the variability of the maximum speed (velocity) of the apparently two flow/branches and their corresponding locations is also analyzed, in order to compare with the study of Fonseca et al. (2004). The goal is also to investigate the variability of the current location with respect to the wind variability and to the tropical Atlantic climate modes. In this study, the presence of two flows of the NBCR and the NECC two-core structure are identified when the velocity profile shows two local maxima separated by a local minimum respectively, in the NBCR region (considered between 4°-10° N) and the NECC region (considered between 3°-11° N) (Fig. 4S4-S6).
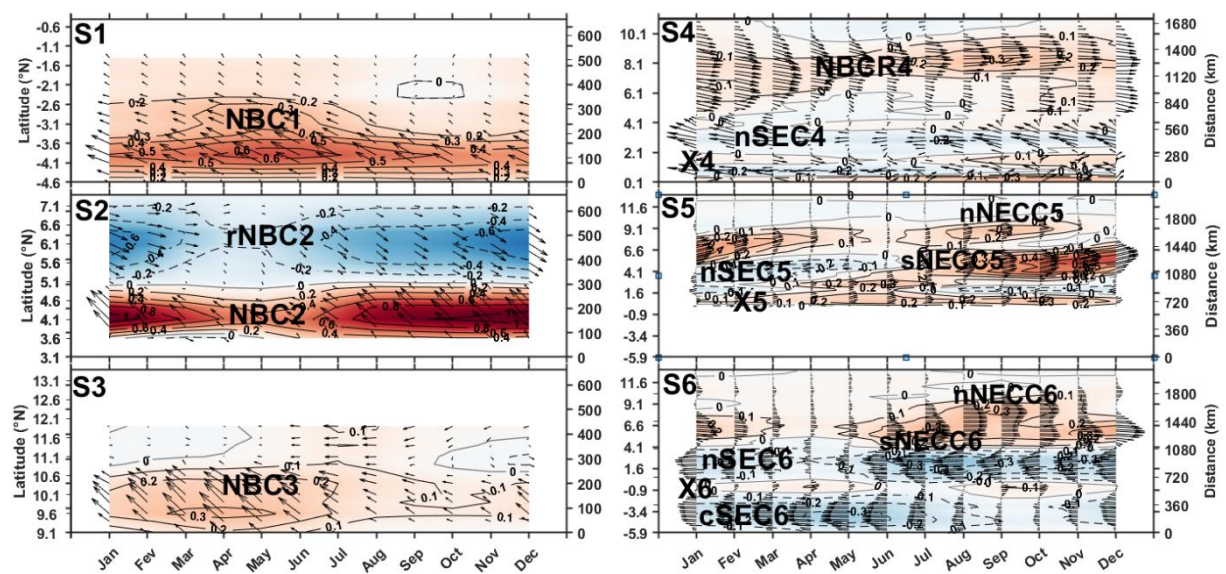
Figure 4. Average seasonal cycle obtained from Figure 3 (vectors of the currents are superimposed on the contour of their amplitude in m s^{-1}). On the right sides of each subplots, the distances from the southernmost point (in km) are indicated.

4   Seasonal variability

Here we focus on the seasonal cycle of the different current branches observed in the study area. Therefore, a monthly climatology of the velocity estimates shown in Fig. 3 is calculated for each of the six sections (Fig. 4). For further analysis, the monthly climatology of Vmax, Vmax location, the current width and the relative current intensity has also been derived from the corresponding monthly time series for different current components (Fig. 5). Ours analyses are presented in the following paragraph from the southeast to the northwest of the study area.
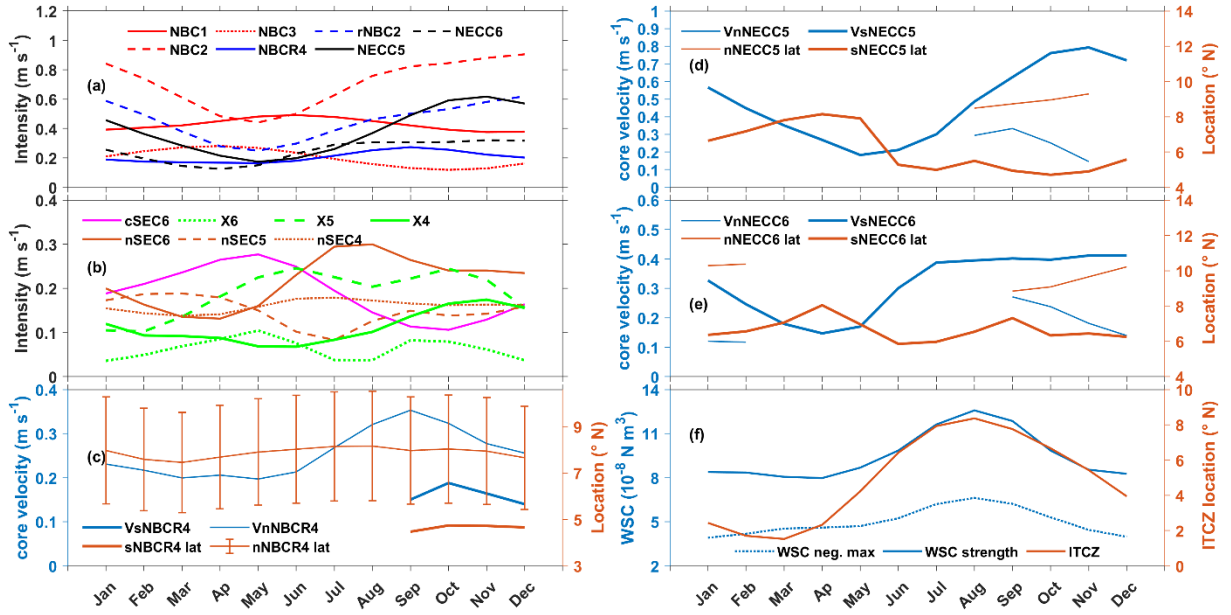
Figure 5. Monthly climatology of: the relative currents' speed (m s^{-1}) **(a-b)**; the cores velocity/location in the NBCR regions **(c)**; the core velocity/location of the NECC branches along sections 5 and 6 **(d-e)**; and the absolute values of the maximum negative wind stress curl (WSC neg. max), the WSC strength and the ITCZ location **(f)**. Acronyms are listed in Table 1 and the numbers next to the acronyms represents the number of the sections. On **(c)**, **(d)** and **(e)**, the the core velocities and locations are respectively, in blue and orange color.

4.1 The North Brazil Current and its retroflection

In Fig. 4, the NBC (Section 1) and the cSEC (Section 6) are observed both located at ~ 4° S and present similar seasonal cycles, with stronger flows during the first half of the year. The cSEC6 velocity maximum (0.3 m s^{-1}) / minimum (0.1 m s^{-1}) appears in May/October, respectively. The NBC1 velocity maximum (0.6 m s^{-1}) / minimum (0.4 m s^{-1}) appears in May-June/November-December (Fig. 5a). These annual cycles are also similar to the annual cycle of the NBUC transport observed by Rodrigues et al. (2007) at 10° S and which is related to the bifurcation location of the sSEC. This suggests that at its southernmost location, the seasonal variability of the NBC might be partly driven by the location of the sSEC bifurcation, which has been shown to be influenced by the annual cycle of the WSC over the area 5°–10° S, 25°–40° W (Rodrigues et al., 2007).

When comparing the NBC along sections S1, S2, S3 and S4 (Fig. 4S1-S4 and Fig. 5), it clearly depicts two different seasonal cycles along its northward path. The NBC2, NBCR4 and the rNBC2 flows show approximately the same seasonal cycles, in opposite phase with NBC1 and NBC3 ones, approximatively in phase. NBC2 is narrower but relatively stronger than NBC1. It decreases from January to May (by ~ 0.4 m s^{-1}), and then increases again to reach a maximum in November-December (1 m s^{-1}). Compared to NBC2, the rNBC2 is broader (width of ~ 350

km against 200 km) but less intense (maximum of 0.6 m s^{-1} in November-December). Apparently, the NBC2 width and strength seem to be linked to the nSEC intensity in the eastern basin (see nSEC6 and nSEC4 in Fig. 5b). When the nSEC is weaker, the NBC2 is also weaker and narrower. Then, the NBC2 starts growing one month later when the nSEC intensity is increasing. This shows the importance of the nSEC contribution to the NBC to the north of the equator. The delay between the nSEC and NBC2 growth can be due to the mesoscale activities more intense in the western basin (Aguedjou et al., 2019). The fact that the NBC1 and the NBC3 are in phase when the nSEC contribution to the NBC2 is lower might also indicate that the NBC is more stable when the intrusion of water from the nSEC is weak. And then, most of the NBC in the upper layer tends to follow its northward route. Contrariwise, when the current is unstable because of the barotropic and baroclinic instabilities generated by the nSEC, most of the NBC flow tends to retroflects eastward. This can justify the phase of the NBC2, NBC4 and rNBC2. In Fig. 4, from September to January, we observe two retroflections of the NBC: the main one around 8°N and a secondary one more to the south, between 4-6° N (Fig. 4S4 and 5c). The flow of this secondary retroflection (called sNBCR) reaches its maximum intensity in October while the main retroflection flow (called nNBCR) reaches its maximum one month earlier. Then, it migrates northward to join the nNBCR4; and both are completely merged at the beginning of the following year (Fig. 4S4). Both branches merge at the beginning of the year and the NBCR then weakens to reach its minimum intensity in May. Note that the seasonal cycles of the NBC2 and the NBCR are similar to the one of the NBC transport obtained by Johns et al. (1998) and Garzoli et al. (2004) using acoustic Doppler current profilers (ADCP)/Inverted Echos sounders/Pressure gauge data. Johns et al. (1998) related the seasonal cycle of the NBC observed in this area to the remote wind stress curl forcing across the tropical Atlantic. Here, we also see that the seasonal cycles of the NBC branches north of the equator (except the NBC continuity along the Guyana coast) seems to follow the remote wind stress curl strength with a delay of one to four months (Fig. 5a-f). Because of the instabilities of the region, the delay should be impacted by the mesoscale activities and/or wave propagations in the region (Fonseca et al., 2004). The northernmost location of the nNBCR maximum intensity occurs in August, when the maximum WSC strength is reached (Fig. 5c, f). The root mean square (rms) of the monthly mean values of its location (Fig. 5c) is nearly constant (~2.3°), and is consistent with the evidence that there may not be a preferred season for NBC ring formation (Garzoli et al., 2003; Goni and Johns, 2003). Indeed, Garzoli et al. (2003) have shown using inverted echo sounder observations that there was a link between the rapid northward/southward extension of the NBC retroflection and the shedding of the rings in this region.

397   Farther north, the NBC component flowing along the Guyana coast (NBC3) is twice wider (~

398   440 km) and less intense than the NBC2 (Fig. 4S2-S3). It reaches a minimum in October (~ 0.1

399   m s^{-1}), and a maximum during March-May (0.3 m s^{-1}) when the NBCR4 is minimum (Fig. 4S3-

400   S4 and 5). As already mentioned, its seasonal cycle is similar to the NBC1 and cSEC, and might

401   also be influenced by the sSEC bifurcation location.

4.2   The North Equatorial CounterCurrent

403   The NECC (both NECC5 and NECC6) seasonal cycle is similar to the ones of the NBC2,

404   NBCR4 and rNBC2 (Fig. 4S2, S4, S5-S6). It weakens along its pathway and its intensity is

405   maximum in November-December (~ 0.6 m s^{-1} at 42° W and ~ 0.3 m s^{-1} at 32° W), and

406   minimum in April-May (Fig. 5a). During the second part of the year, we observe the two-core

407   structure previously investigated by Urbano et al. (2006; 2008). The two cores/branches are

408   seen first at 42° W in August, then at 32° W in September (Fig. 4 and 5d-e). The northern

409   branch (nNECC) is narrower (located between 7°-9° N) and stronger (0.3 m s^{-1}) in August-

410   September at 42° W (Fig. 4S5 and 5d). It is even separated from the southern branch from

411   October to December. At 32° W, the NECC appears with one single core from September

412   (northern core velocity of ~ 0.2 m s^{-1}) to November. The northern core is gradually decreasing

413   in intensity and shifting northward until forming a separated second branch, which is located

414   between 9-11° N from December to February, and then becomes very weak in March-April

415   (Fig. 4S5 and 5e). From June to July, the NECC signature (sNECC branch) is located between

416   3-4° N at 42° W, and is connected from the south to the eastward flow associated with X5 in

417   Fig. 4S5. Urbano et al. (2008) showed with ADCP data at 38° W that the eastward NECC cycle

418   may start in this region when the EUC is shallower and further north, and seems to be connected

419   also to a shallower NEUC during this period of the year. The presence of the equatorial surface

420   eastward flow X5 suggests that this latter may be the one that favors the surfacing and the

421   connection of both currents during June-July. From June to November, the sNECC branch

422   increases simultaneously with the rNBCR2. However, it reaches its maximum one month earlier

423   (November) and start decreasing when the rNBC is still increasing. This confirms that the

424   NECC is not only fed by the rNBC at the surface as suggested by Verdy and Jochum, 2005.

425   The sNECC witnesses the same variability at both 32° W and 42° W, but reaches its minimum

426   early in March-April at 32° W when the climatological NECC is described in the literature as

427   a reversing flow or is missing at its usual location (Garzoli and Katz, 1983; Garzoli, 1992). At

428   this location (32° W), the sNECC starts increasing from April-May, between 4°-6° N far from

429   the eastward flow X, and grows until November. Burmeister et al. (2019) showed that, in the

central Atlantic, when the ITCZ migrates northward (April to August) (Fig. 5f), the nSEC recirculates eastward to reach the NEUC which then increases. The presence of the sNECC flow in April-May may suggest that the NECC flow might be initiated by an eastward recirculation of the nSEC which flows on top of the NEUC during this period. It reaches its first maximum in July-August together with the nSEC, and a second maximum in November (Fig. 5a, b, e). At 32° W and 42° W the sNECC shows two northward migrations. The first migration occurs from June-July (June) to August (September) at 42° W (32° W), and the second occurs from October to April (Fig. 5d-e). Fonseca et al. (2004) also found such behaviors but with some differences: two northernmost NECC locations in February and August, and two southernmost NECC locations in June and December. But they lacked data between March and May, and we do not use the same methods to compute the core position.

4.3 The central and northern branches of the South Equatorial Current

Obviously, the cSEC and nSEC which are two branches of the westward SEC do not have the same seasonal cycle (Fig. 4S4, S5, S6). This is due to the fact that, in the northern hemisphere, the nSEC is affected by the southerlies which cross the equator, inducing a migration of the ITCZ location. However, the cycles of the nSEC4, nSEC5 and nSEC6 have maxima at different periods of time. At 32° W, the nSEC (nSEC6) increases from April to reach a maximum of ~ 0.3 m s^{-1} in August, following the migration of the ITCZ (Fig. 5b, f). During this time, at 42° W, the nSEC (nSEC5) migrates northward, and its intensity decreases until July, when it almost disappears. The eastward flow X then appears (Fig. 4S5). The nSEC5 is observed again after July, increases and reach a maximum of ~ 0.2 m s^{-1} in March (Fig. 4S5, S6 and Fig. 5b). Over the continental shelf, most of the nSEC joins the NBC (section 4, around 2-4° N and 46° W) and a part deviates southeastward to join the rNBC and form the eastward flow X4 (captured along section 4, Fig.4S4). The nSEC component that joins the NBC reaches its maximum of ~ 0.2 m s^{-1} between June and August (also following the ITCZ northward migration, Fig. 5b, f). However, the nSEC seasonal variations are relatively small (~ 0.15 m s^{-1}) (Fig. 4S4). It is particularly true for nSEC4 but the angle of the section relative to the flow probably leads to a significant reduction of the current amplitude captured.

4.4 The eastward current X

Figure 4S4-S6 show the presence of an eastward current near the equator. Such feature was already observed and mentioned by Hisard and Hénin (1987) and Bourles et al. (1999b) using hydrographic and ADCP data. In Fig. 4S4, eastward flows are captured between 1-2° N (X4) and along the equator. As mentioned in Sect. 4.3, they may be composed of the part of the nSEC

that does not join the NBC and the rNBC (which is known to feed the EUC in the thermocline layer). The weaker intensity of X4, compared to X5 (i.e. X at 42) is explained by the angle between S4 and the current direction. But the weaker intensity of X6 (i.e. X at 32° W) is due to the weakening of the corresponding eastward flow between both longitudes. X4 and X5 are observed almost throughout the year (Fig. 4S4-S6) and their amplitude follows a semi-annual cycle (Fig. 5b) similar to the EUC in the eastern Atlantic (Hormann et al. 2007). However, the periods of the maxima are slightly different from one location to the other. X4 displays a semi-annual cycle, with a weak maximum in March-April ($\sim$ 0.1 m s^{-1}) and another maximum in November ($\sim$ 0.2 m s^{-1}). X5 amplitude is larger because of the merging of X4 with the eastward flow observed along the equator (Fig. 4S5). Its maxima occur in June and October with similar intensity (more than 0.2 m s^{-1}) (Fig. 5b). X6 (at 32° W) is weaker, but reaches its maxima in May and September-October (less than 0.1 m s^{-1}). Since this eastward X flow is almost not documented in the literature, we will come back to it in Sect. 6.

5   Interannual variability

Beyond the dominant seasonal variability of the circulation at regional scale, we also observe a year-to-year variability of the surface velocities in the study area (Fig. 2 and Fig. 3). The latter is analyzed here, using the time series of the characteristics of the different current branches (see end of Sect. 3) captured along the 6 sections (Fig. 6). We will also analyze this variability in the light of the tropical Atlantic climate modes.

In Fig. 6a-b we observe that over the whole study period the intensities of the cSEC6 (cSEC along section 6) and of the NBC1 (NBC along section 1) and NBC2 (NBC along section 2) vary between 0.05-0.35 m s^{-1}, 0.3-0.6 m s^{-1} and 0.2-1.2 m s^{-1}, respectively. with corresponding mean values of 0.2 m s^{-1} ± 0.06, 0.4 m s^{-1} ± 0.06 and 0.7 m s^{-1} ± 0.2. To the north, when crossing section 3, the NBC weakens and ranges between 0.05-0.43 m s^{-1} with a mean intensity of 0.2 m s^{-1} ± 0.07. In the equatorial region (±5° of latitude), along sections 5/6, the nSEC intensity varies between 0.05-0.3 m s^{-1}/0.1-0.4 m s^{-1}, with a mean value of 0.15 m s^{-1} ± 0.05/0.2 m s^{-1} ± 0.07 (Fig. 6b). The eastward flow X intensity vary between 0.15-0.3 m s^{-1}, 0.05-0.4 m s^{-1} and 0-0.15 m s^{-1} when crossing sections 4, 5 and 6, respectively, with corresponding mean values of 0.12 m s^{-1} ± 0.05, 0.2 m s^{-1} ± 0.07, and 0.06 m s^{-1} ± 0.03.
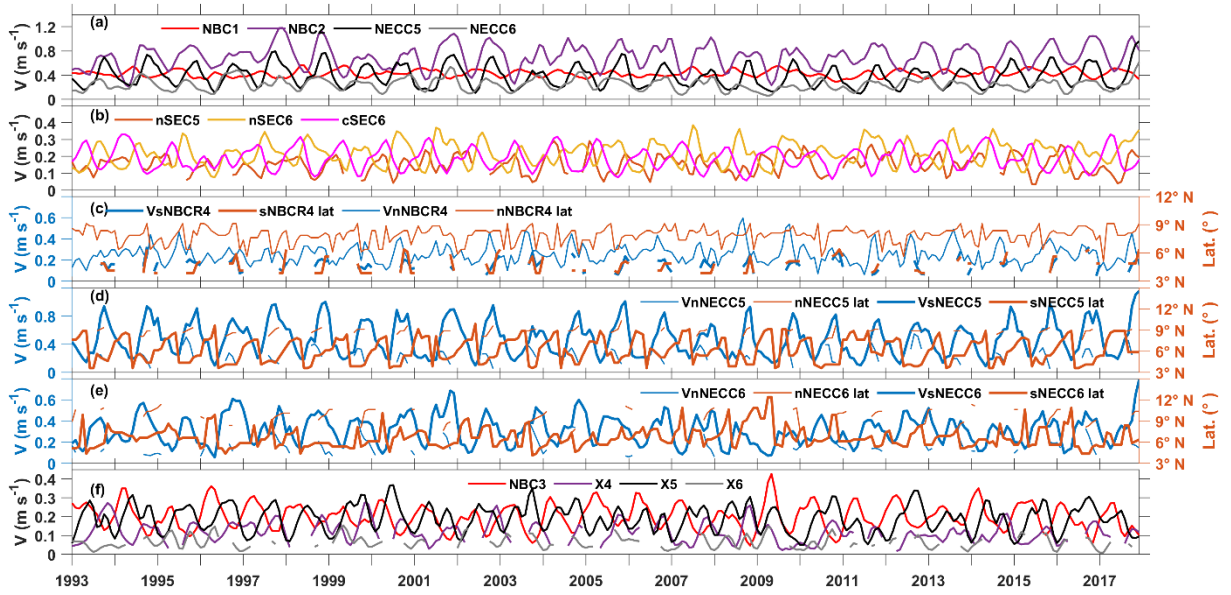
Figure 6. Time series of the 4-month low-pass filtered characteristics of the geostrophic currents **(a-f)** captured along sections 1 to 6. Acronyms are listed in Table 1 and the numbers next to the acronyms represents the number of the sections **(a)**: intensity of NBC1 and NBC2, and of the NECC5 and NECC6. **(b)**: intensity of the cSEC6 and of the nSEC5 and nSEC6. **(c)**, **(d)** and **(e)** core velocities and the locations of respectively the nNBCR4 and the sNBCR4 flows, the nNECC5, the sNECC5, the nNECC6 and the sNECC6. **(f)** Intensity of the NBC3, X4, X5 and X6.

The two-core structure of the NECC and the NBCR regions show the highest year-to-year variations in both velocity and location (Fig. 6c-e). The NECC/NBCR time series were found significantly correlated (>0.98) in terms of both intensity and core velocity (sNECC and nNBCR; figure not shown). At 42° W, the sNECC/nNECC) velocity cores vary between 0.1-1.2 m s^{-1}/0.05-0.55 m s^{-1}, with mean values of 0.5 m s^{-1} ± 0.25 /0.25 m s^{-1} ± 0.1. They are located between 3.6°-9.9° N/7.6°-10.4° N, with mean locations at 6.1° N ± 1.7°/8.9° N ± 0.8° (Fig. 6d). At 32° W, the cores vary between 0.05-0.8 m s^{-1}/0.05-0.5 m s^{-1}, with mean velocities of 0.3 m s^{-1} ± 0.13/0.2 m s^{-1} ± 0.09. They aren located between 4.1°-12.4° N/7.4°-11.6° N, with mean locations of 6.6° N ± 1.4°/9.7° N ± 1.1° (Fig. 7e). The sNBCR /nNBCR maximum speeds crossing the section 4 varies between 0.05-0.3 m s^{-1}/0.05-0.6 m s^{-1}, with mean values of ~ 0.15 m s^{-1} ± 0.06/0.25 m s^{-1} ± 0.08. And, they are located between 3.9°-6.4° N / 5.1°-9.1° N, with mean locations of 4.7° N ± 0.8°/7.9° N ± 0.8°. Northeast of the equator, for all these current branches, we observe important year-to-year variations, both in terms of current core location and of velocity amplitude.

For further analysis, the anomalies of the current's characteristics (intensity and core value/location) relative to their monthly climatology have been computed (Fig. 7). First, we do not see obvious relationship between the different resulting monthly anomaly time series over the whole period investigated. No relationship was found between the intensity of the NECC branches or of the NBCR flows and their location. However, for some particular years, both the NECC intensity/core velocity and location show significant anomalies at 32° W. For example, the monthly anomalies of the sNECC6 location were shifted far to the north / south in 2009 and 2010 / 1996 and 2001. Simultaneously, the monthly anomalies of the sNECC6 intensity/core value were unusually weak / strong (Fig. 7f-g).

To investigate the relationship between the AMM, the AZM, and the year-to-year variability of the characteristics of the different currents at different locations over 1993-2007 period, we computed the three-month average anomalies centered each month of the time series of the current anomalies and of the climate mode indexes (so-called 3-month anomaly time series). So, the AMM and AZM peak events (respectively, March-April-May and June-July-August) have been correlated with the 3-month anomaly time series of the currents in order to learn more about their possible relationship at the interannual timescale in the study area (figures not shown). Only the correlations greater than ±0.5 and which have been found significant with 95 % of confidence level, performing the Student's test are discussed below (listed in Table 3).
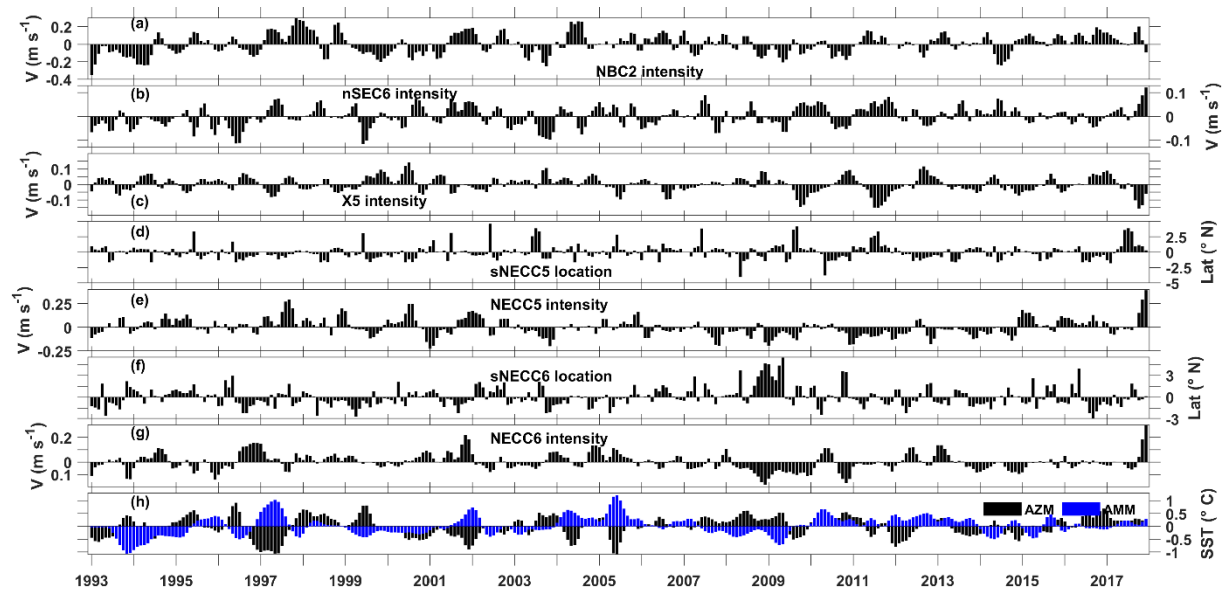
Figure 7. Time series of monthly anomalies relative to the monthly climatology for: **(a)**, the NBC2 intensity; **(b)**, the nSEC6 intensity; **(c)**, the equatorial surface eastward flow X5 intensity; **(d)**, the sNECC5 core location; **(e)**, the NECC5 intensity; **(f)**, the sNECC6 core location; and **(g),** the NECC6 intensity; **(h),** Normalized indexes of the AMM (blue color) and AZM (black color).

Table 3. Correlations values between the characteristics of the current branches and the Atlantic meridional and zonal mode indexes (AMM and AZM, respectively). Where the correlations are found lower than 0.5, we indicate "insignificant" over the whole time period ("none"). The current branches analyzed are the NBC, the sNECC, the nSEC and the equatorial eastward flow called X.

Current branches' characteristics		Atlantic meridional mode (AMM) during March-April-May	Atlantic Zonal mode (AZM) during June-July-August
NBC1 intensity (section 1)	Correlation	Higher than -0.51	Insignificant
	Period	June-July	None
NBC2 intensity (section 1)	Correlation	0.58	Insignificant
	Period	March-April-May	None
sNECC5 intensity (section 5)	Correlation	Insignificant	-0.51
	Period	None	September
sNECC6 intensity (section 6)	Correlation	Higher than 0.50	Insignificant
	Period	March-April-May	None
sNECC6 core location (section 6)	Correlation	Higher than 0.51	Insignificant
	Period	March-April-May	None
nNECC6 core location (section 6)	Correlation	-0.62	Insignificant
	Period	March	None
nSEC5 intensity (section 5)	Correlation	Insignificant	-0.52
	Period	None	November
nSEC6 intensity (section 6)	Correlation	Higher than 0.52	Insignificant
	Period	March-April-May	None
Equatorial eastward flow X (Sections 4 and 5)	Correlation	Higher than -0.55	Insignificant
	Period	May-June	None
Equatorial eastward flow X (Section 6)	Correlation	Higher than 0.62	Higher than -0.52
	Period	March-April-May	June-July

The AMM index is found anticorrelated with the NBC intensity along the section 1 during March-April-May, the nNECC core location along the section 6 and the equatorial eastward flow (X) intensity west of 42° W, with respective coefficient of correlation (cc) higher than -0.51 during June-July, about -0.62 in March, and higher than -0.55 in May-June. These anti-correlations show the probability of the positive (negative) AMM phases to lead the negative (positive) anomalies of the nNECC core location at 32° W with 0-month delay, the negative (positive) NBC intensity between 3°-5° S and the X flow intensity anomalies (west of 42° W) with 1- to 2-month and 0- to 1-month delay, respectively. However, the AMM index during March-April-May is found correlated with the NBC intensity north of the equator before the retroflection (cc ~0.58) and, the sNECC intensity/core location and the nSEC intensity at 32°

W (cc higher than 0.50/0.51 and cc higher than 0.52, respectively) during the same period of time. This suggests that the positive (negative) AMM phases probably drives the positive (negative) anomalies of the corresponding currents with no time lag.

During June-July-August, the AZM index is found anticorrelated with the sNECC/nSEC intensity at 42° W (cc=-0.51/-0.52) only in September/November. This suggests that the positive (negative) AZM phases probably lead the negative (positive) anomalies of the sNECC/nSEC intensity with 1- and 3-month delay, respectively.

The eastward flow X intensity at 32° W is found simultaneously correlated with AZM and AMM in June-July and March-April-May, with cc higher than 0.62 and -0.52, respectively. This suggests that the positive (negative) anomalies of X at 32° W might be associated with both positive (negative) AZM and negative (positive) AMM phases with no delay.

Referring to Cabos et al. (2019), the relationships found between the currents and the AMM show the influence of the strengthening of the southeast trade winds on the southward migration of the nNECC core at 32° W, whereas the NBC intensity between 3°-5° S and the equatorial eastward flow X intensity west of 42° W decrease, and vice versa. Conversely, the strengthening of the southeast trade winds may influence the northward migration of the sNECC core at 32° W, whereas the NBC2, sNECC6 and nSEC6 intensities increase, and vice versa. Referring to the same authors, the relationship with the AZM indicates the probable influence of the positive westerlies anomalies in the western part of the basin on the negative anomalies of the sNECC and nSEC intensities at 42° W, and vice versa. Concerning the eastward flow X at 32° W the relationship with both the AZM and the AMM modes indicate its strengthening during the concurrent events of positive westerlies anomalies in the western part of the basin and the negative southerlies winds anomalies, and vice versa.

6   Discussion

Finally, we have computed the seasonal maps of the geostrophic currents in the whole WTA (Fig. 8) in order to have a regional view of the seasonal variations of the circulation. Fig. 8 confirms the results obtained from the analysis of the cross-section velocities in Sect. 4 (in terms of seasonal cycles and spatial structure) but also highlights interesting new features.

A large cyclonic circulation is observed between 35°-45° W and 0°-5° N during boreal spring (blue ellipse). The latter is formed by the westward nSEC which is suddenly deviated to the northeast by the presence of an eastward flow at ~32° W. Then, near 44° W and 5° N, the nSEC

meets the rNBC which reaches it southernmost position during this season, and deviates to the southeast. When reaching the equatorial region between 0°-2° N, where the equatorial eastward flow is found (Fig. 4), the resulting flow becomes stronger, and is deviated to the east, close this cyclonic feature. This finding might answer the question of Schott et al. (1998) about the destination of the rNBC during spring, when the rNBC does not feed the NECC anymore. From German cruises SADCP measurements (downloaded from the data center PANGEA https://doi.pangaea.de/10.1594/PANGAEA.937809 and described in Tuchen et al, 2022), the zonal and meridional components of currents over the equatorial region have been analyzed (40°W, 35°W and 32°W: figures in supplementary material). They confirm the existence of the equatorial surface eastward flow, with a shifting tendency at 35°W to the north. During the boreal winter, another cyclonic circulation is observed between 44°-50° W and 5°-10° N (blue ellipse in Fig. 8): part of the NECC recirculates north-westward to join the rNBC. During both boreal winter and spring, south-westward recirculations of the NECC appear to strengthen the nSEC located west of 32° W. This is consistent with the increase of the nSEC intensity observed along section 4, compared to the nSEC intensity captured along section 6, between February and May (Fig. 5b).

During the second half of the year, Fig. 8 shows a wider NECC which extends north of 10°N. During boreal fall, the NECC flow is formed by a nNECC branch separated from the initial sNECC branch during between 38°-48° W, that meet east of 38° W. This is consistent with Fig. 4 S5-S6. During boreal summer, the nNECC branch seems to be supplied by the northern part of the NBC retroflection. This connection seems to fade during boreal fall.

In the equatorial region (2° S-2° N), Fig. 8 also shows an equatorial eastward flow X with lower amplitude which appears to be extended east of 32° W and stronger during boreal spring and fall. This feature can be related to the near-surface eastward flow mentioned by Hisard and Hénin (1987) and Bourlès et al. (1999b) on top of the EUC in the WTA. Hisard and Hénin (1987) explained the poor description of this current in the literature by the difficulty of ADCP measurements to fully capture the upper layer currents in this area. They showed that this near-surface current, independent from the EUC, can reach amplitudes larger than 0.5 m s^{-1} between 23° W and 28° W. In this study, the seasonal maps of the near-surface Ekman currents (figure not shown) showed westward currents with higher amplitudes in this equatorial band (larger than 0.2 m s^{-1}) compared to X, mostly east of 32°W. Then, we conclude that the near-surface velocities found here in the equatorial region should be underestimated, particularly in the eastern basin. This is consistent with the strengths of the X current found in Fig. 5b.

For the first time, the seasonal cycle of the equatorial eastward flow has been analyzed in Sect. 4.4 of this study (Fig. 4S4, S5, S6 and Fig. 5b). It is similar to the seasonal cycle of the EUC (semi-annual cycle with two maximum), which might be due to the fact that most part of the flow is fed by the rNBC.
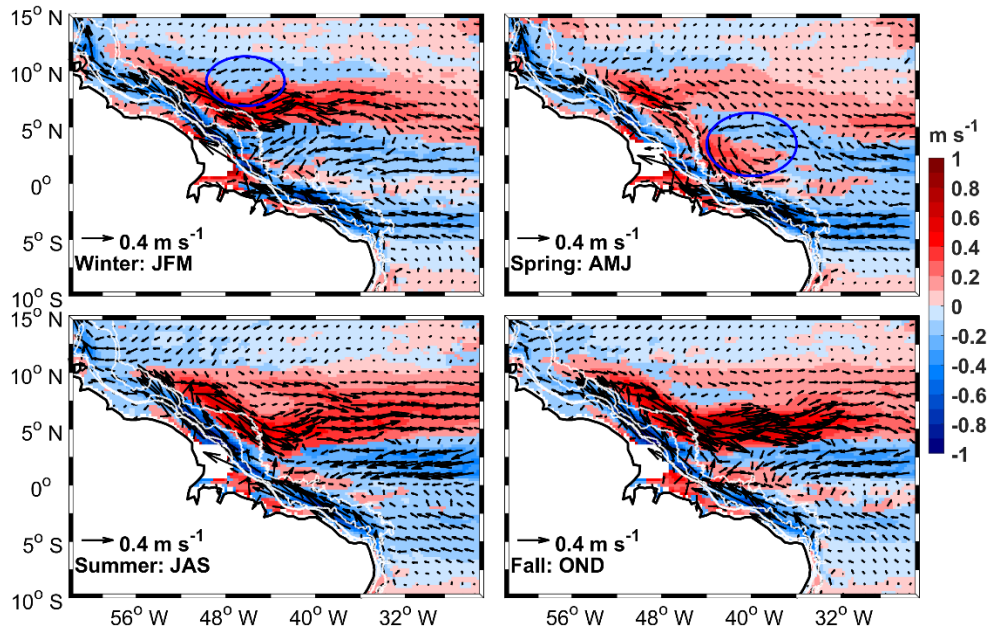
Figure 8. Seasonal maps of the geostrophic currents in the western tropical Atlantic over the 1993-2017 period for boreal winter (top left panel: JFM for January-February-March), boreal spring (top right panel: AMJ for April-May-June), boreal summer (bottom left panel: JAS for July-August-September:) and boreal fall (bottom right panel: OND for October-November-December:). The velocity vectors are superimposed on the speed multiplied by the sign of their zonal components (m s^{-1}). The two cyclonic circulations observed during boreal winter and spring are indicated by blue ellipses. The white lines near to the continent are from west to east, the 300 m, 1000 m, 3000 m and 4000 m isobaths.

From the analyses of the current carried out above, we propose a new scheme of the seasonal variations of the western boundary tropical Atlantic circulation (Fig. 9). The new current branches found in this study are indicated in green and the currents coming from the north/south are in blue/orange. The width of the current arrows is proportional to the current amplitude and the dotted arrows represent the currents with the minimum amplitudes. C1 and C2 are for respectively, the cyclonic circulations highlighted between 44°-50° W and 35°-45° W.

639
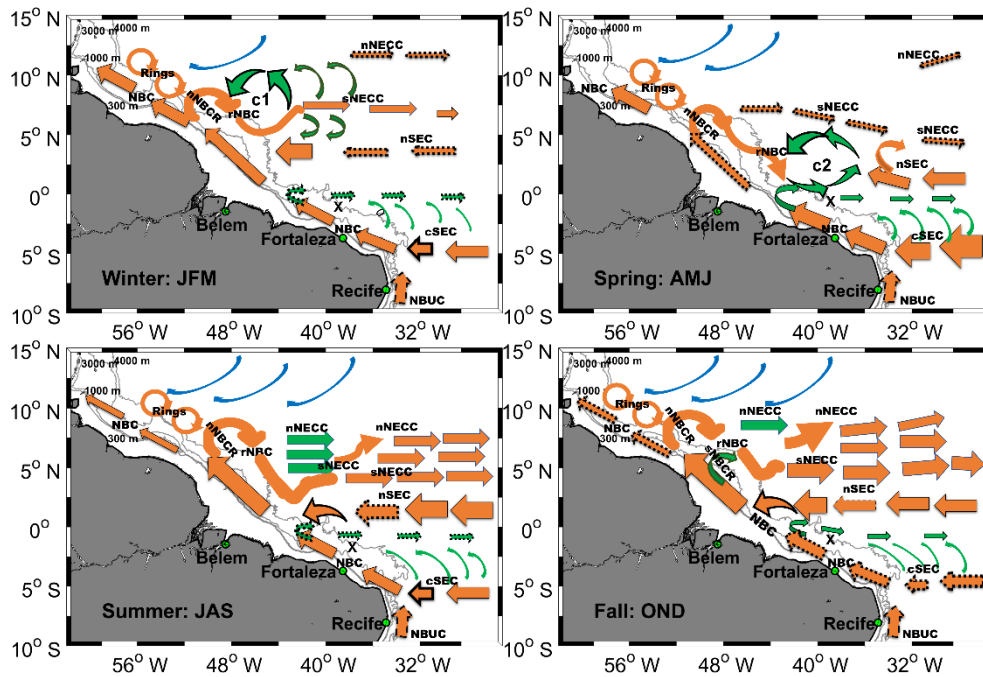
Figure 9. Schematic view of the seasonal maps of the tropical western boundary circulation. C1 and C2 represent the cyclonic circulations highlighted in this study. The wider (dotted thin) arrows show current branches with maximum (minimum) intensity. The subsurface NBUC is represented by dashed arrows. The already known current branches are in orange/blue. The green arrows characterize the new branches observed. NBC is the North Brazil Current; nNBCR and sNBCR are the northern and the southern flows of the North Brazil Current retroflection, respectively; rNBC is the retroflected branch of North Brazil current; nNECC and sNECC are the northern and the southern branches of the North Equatorial Countercurrent (NECC), respectively; cSEC and nSEC are the central and the northern branches of the South Equatorial Current (SEC), respectively.

Concerning the interannual variability, Hormann et al. (2012), based on the analyses of 17 year of altimetry and drifter' data, found interesting scenarios about the NECC spatial and temporal variability. However, they did not separate the sNECC from the nNECC. In their study, the authors have associated the strengthening of the NECC in the whole basin to the negative phase of the AZM, and its northward shift to the positive phase of the AMM. Our results show different behaviors of the NECC system as a function of the branch and core location. We also showed possible relationships between the southern NECC branch intensity and location with the AMM phases at 42° W, and conversely a possible relationship between the southern NECC branch intensity and location with the AZM phases at 32° W. These results open the way to deeper investigations in future studies.

7   Summary and Perspectives

Twenty-five years (1993-2017) of gridded altimetry data from CMEMS were used to improve the description of the seasonal and interannual variations of the western boundary circulation of the tropical Atlantic. To do so, a new approach based on the calculation of the current intensity was applied to six horizontal sections defined. These sections have been designed to intersect the path of the principal upper ocean flows over the west tropical Atlantic. Copernicus Climate Service ERA5 wind estimates and the NOAA OI SST v2 product were also used to investigate the possible link between the variability of the regional circulation and the large-scale remote wind forcing on one hand, and the tropical Atlantic climate modes on the other hand.

Our results highlight a complex regional circulation, with significant seasonal and year-to-year variations of the current's intensity and location. South of the equator, we observe a stronger/weaker central branch of the South Equatorial Atlantic (cSEC) and of the North Brazil Current (NBC) during boreal spring/fall. North of the equator, the NBC component flowing along the Guyana coast exhibits a similar annual cycle. However, between both, the NBC part located before the retroflection is out of phase (i.e. stronger during summer-fall), when fed by the northern branch of the South Equatorial Current (nSEC). Its larger amplitudes appear during boreal fall, 3-4 months after the maximum of the remote wind stress curl (WSC) strength (in August). The North Equatorial Countercurrent (NECC) is connected with the retroflected branch of the NBC, and both show similar annual cycle. A secondary North Brazil Current Retroflection (NBCR) was observed for the first time during boreal fall in this study: it is located between 4°-6° N. The two-core/branch structure of the NECC during the second half of the year was also confirmed and analyzed separately. Between 0°-5° N and 35°-45° W, a surface cyclonic circulation develops during boreal spring. It is found to initiate the growth of the NECC at 42° W in June. However, at 32° W, the NECC doesn't show any connection with this cyclonic circulation, but starts its seasonal cycle earlier in April when the ITCZ migrates northward and the remote WSC strengthens. In the equatorial region, between 2° S-2° N, the geostrophic currents show the presence of an equatorial surface eastward flow which has a seasonal cycle similar to the Equatorial Undercurrent (EUC). But the near-surface Ekman currents have to be taken into account here to have a good description of the surface circulation.

Concerning the interannual variability, it is much weaker than the seasonal one. We do not observe an obvious picture at regional scale but it is more important in the eastern part of the basin. The analysis of the changes in characteristics of the different current branches (intensity

692 and core location), with respect to the tropical Atlantic climate modes, shows different possible
693 scenarios associated with one or both modes. It opens the way to further investigations
694 concerning the link between the Atlantic climate modes (ACM) and the current transports, not
695 possible with altimetry alone.

696 As a conclusion, this study demonstrates the ability of altimetry to characterize the seasonal
697 and interannual variability of the surface circulation in the study area. It confirms previous
698 findings but also significantly complements the knowledge of the different currents at regional
699 scale. Combined use of regional modelling, altimetry and in-situ observations will allow us to
700 go further in the understanding of the spatial and temporal structure of the regional circulation.
701 The intraseasonal variability, significant in the near-shore region of the study area (Fig. 2d) is
702 not studied here. It will be the subject of a future work, based on a coastal altimetry product
703 that will allow a significantly better resolution and accuracy along the continental shelf,
704 compared to a gridded product.

Authors contribution

706 Djoirka M. Dimoune performed the data analyses as part of his PhD thesis. Florence Birol,
707 Fabrice Hernandez, Fabien Leger and Moacyr Araujo supervised this research.

Competing interests

709 The authors declare that they have no conflict of interest.

Acknowledgements

711 This work has been supported by: CAPES Foundation who funded the thesis of the first author,
712 CAPES-Print (grants 88887.467360/2019-00) who funded his visit to LEGOS during the first
713 six months spent in the laboratory, and LEGOS and the CNES/TOSCA program as part of
714 SWOT-Brésil project that funded the three last months of extension in the laboratory. The
715 authors thank the CMEMS, who processed the geostrophic currents data and made them
716 available. They thank also the ECMWF and NOAA respectively who made available the mean
717 wind fields data and SST for the work. Thank also the two reviewers of this paper for their
718 helpful suggestions and corrections which helped to improve and make this work more
719 understandable. This work represents collaboration by the INCT AmbTropic, the Brazilian
720 National Institute of Science and Technology for Tropical Marine Environments,

CNPq/FAPESB (grants 565054/2010-4 and 8936/2011 and 465634/2014-1) and the Brazilian Research Network on Global Climate Change FINEP/Rede CLIMA (grants 01.13.0353-00). This is also a contribution to the LMI-TAPIOCA and to the TRIATLAS project, which has received funding from the European Union's Horizon 2020 research and innovation program under grant agreement No 817578

References

Aguedjou, H. M. A., Dadou, I., Chaigneau, A., Morel, Y., and Alory, G.: Eddies in the Tropical Atlantic Ocean and their seasonal variability, Geophys. Res. Lett., *46*(21), 12156-12164, https://doi.org/10.1029/2019GL083925, 2019.

Araujo, M., Noriega, C., Hounsou-Gbo, G. A., Veleda, D., Araujo, J., Bruto, L., Feitosa, F., Flores-Montes, M., Lefèvre, N., Melo, P., Ostuska, A., Travassos, K., Schwamborn, R., Neumann-Leitão, S.: A synoptic assessment of the amazon river-ocean continuum during boreal autumn: From physics to plankton communities and carbon flux, Front. Microbiol., 8, 1358, https://doi.org/10.3389/fmicb.2017.01358, 2017.

Arbic, B. K., Scott, R. B., Chelton, D. B., Richman, J. G., and Shriver, J. F.: Effects of stencil width on surface ocean geostrophic velocity and vorticity estimation from gridded satellite altimeter data, J. Geophys. Res.-Oceans, 117(C3), https://doi.org/10.1029/2011jc007367, 2012.

Aroucha, L. C., Veleda, D., Lopes, F. S., Tyaquiçã, P., Lefèvre, N., and Araujo, M.: Intra-and Inter-Annual Variability of North Brazil Current Rings Using Angular Momentum Eddy Detection and Tracking Algorithm: Observations From 1993 to 2016, J. Geophys. Res.-Oceans, 125(12), e2019JC015921, https://doi.org/10.1029/2019jc015921, 2020.

Burmeister K., Lübbecke, J. F., Brandt, P., and Duteil, O.: Interannual variability of the Atlantic North Equatorial Undercurrent and its impact on oxygen, J. Geophys. Res.-Oceans, 124, 2348–2373, https://doi.org/10.1029/2018JC014760, 2019.

Bourles, B., Molinari, R. L., Johns, E., Wilson, W. D., and Leaman, K. D.: Upper layer currents in the western tropical North Atlantic (1989–1991), J. Geophys. Res.-Oceans, 104(C1), 1361-1375, https://doi.org/10.1029/1998jc9000250, 1999.

Bourlès, B., Gouriou, Y., and Chuchla, R.: On the circulation in the upper layer of the western equatorial Atlantic, J. Geophys. Res.-Oceans, 104(C9), 21151-21170, https://doi.org/10.1029/1999jc900058, 1999.

Brandt, P., Schott, F. A., Provost, C., Kartavtseff, A., Hormann, V., Bourlès, B., and Fischer, J.: Circulation in the central equatorial Atlantic: Mean and intraseasonal to seasonal variability, Geophys. Res. Lett., 33(7), https://doi.org/10.1029/2005gl025498, 2006.

Brandt, P., Claus, M., Greatbatch, R. J., Kopte, R., Toole, J. M., Johns, W. E., and Böning, C. W.: Annual and semiannual cycle of equatorial Atlantic circulation associated with basin-mode resonance, J. Phys. Oceanogr., 46(10), 3011-3029, https://doi.org/10.1175/jpo-d-15-0248.1, 2016.

Cabos, W., de la Vara, A., and Koseki, S.: Tropical Atlantic variability: observations and modelling, Atmosphere, 10(9), 502, https://doi.org/10.3390/atmos10090502, 2019.

Cochrane, J. D., Kelly Jr, F. J., and Olling, C. R.: Subthermocline countercurrents in the western equatorial Atlantic Ocean, J. Phys. Oceanogr., 9(4), 724-738, https://doi.org/10.1175/1520-0485(1979)009<0724:scitwe>2.0.co;2, 1979.

Didden, N., and Schott, F.: Seasonal variations in the western tropical Atlantic: Surface circulation from Geosat altimetry and WOCE model results, J. Geophys. Res.-Oceans, 97(C3), 3529-3541, https://doi.org/10.1029/91jc02860, 1992.

Dossa, A. N., Silva, A. C., Chaigneau, A., Eldin, G., Araujo, M., and Bertrand, A.: Near-surface western boundary circulation off Northeast Brazil, Prog. Oceanogr., 190, 102475, https://doi.org/10.1016/j.pocean.2020.102475, 2021.

Ffield, A.: North Brazil current rings viewed by TRMM Microwave Imager SST and the influence of the Amazon Plume, Deep-Sea Res. Pt. I, 52(1), 137-160, https://doi.org/10.1016/j.dsr.2004.05.013, 2005.

Fonseca, C. A., Goni, G. J., Johns, W. E., and Campos, E. J.: Investigation of the north Brazil current retroflection and north equatorial countercurrent variability, Geophys. Res. Lett., 31(21), https://doi.org/10.1029/2004gl020054, 2004.

Fratantoni, D. M., Johns, W. E., Townsend, T. L., and Hurlburt, H. E.: Low-latitude circulation and mass transport pathways in a model of the tropical Atlantic Ocean, J. Phys.

778   Oceanogr., 30(8), 1944-1966,

779   https://doi.org/10.1175/15200485(2000)030<1944:LLCAMT>2.0.CO;2, 2000.

780   Garzoli, S. L., and Katz, E. J.: The forced annual reversal of the Atlantic North Equatorial

781   Countercurrent, J. Phys. Oceanogr., 13(11), 2082-2090, https://doi.org/10.1175/1520-

782   0485(1983)013<2082:tfarot>2.0.co;2, 1983.

783   Garzoli, S. L.: The Atlantic North Equatorial Countercurrent: Models and observations, J.

784   Geophys. Res.-Oceans, 97 (C11), 17931-17946, https://doi.org/10.1029/92jc01363, 1992.

785   Garzoli, S. L., Ffield, A., and Yao, Q.: North Brazil Current rings and the variability in the

786   latitude of retroflection, Elsevier Oceanogr. Ser., 68, 357-373, https://doi.org/10.1016/s0422-

787   9894(03)80154-x, 2003.

788   Garzoli, S. L., Ffield, A., Johns, W. E., and Yao, Q.: North Brazil Current retroflection and

789   transports, J. Geophys. Res.-Oceans, 109(C1), https://doi.org/10.1029/2003jc001775, 2004.

790   Garzoli, S. L., and Matano, R.: The South Atlantic and the Atlantic meridional overturning

791   circulation, Deep-Sea Res. II, 58(17-18), 1837-1847,

792   https://doi.org/10.1016/j.dsr2.2010.10.063, 2011.

793   Gill, A. E., and Adrian, E.: Atmosphere-ocean dynamics, Vol. 30, Academic press,

794   https://doi.org/10.1016/s0074-6142(08)60025-x, 1982.

795   Góes, M., and Wainer, I.: Equatorial currents transport changes for extreme warm and cold

796   events in the Atlantic Ocean, Geophys. Res. Lett., 30(5),

797   https://doi.org/10.1029/2002gl015707, 2003.

798   Goes, M., Molinari, R., da Silveira, I., and Wainer, I.: Retroflections of the north brazil

799   current during february 2002, Deep-Sea Res. Pt. I, *52*(4), 647-667,

800   https://doi.org/10.1016/j.dsr.2004.10.010, 2005.

801   Goni, G. J., and Johns, W. E.: Synoptic study of warm rings in the North Brazil Current

802   retroflection region using satellite altimetry, Elsevier Oceanogr. Ser., 68, 335-356,

803   https://doi.org/10.1016/s0422-9894(03)80153-8, 2003.

804   Hazeleger, W., and De Vries, P.: Fate of the Equatorial Undercurrent in the Atlantic, Elsevier

805   Oceanogr. Ser., 68, 175-191, https://doi.org/10.1016/s0422-9894(03)80146-0, 2003.

806 Hazeleger, W., de Vries, P., and Friocourt, Y.: Sources of the Equatorial Undercurrent in the

807 Atlantic in a high-resolution ocean model, J. Phys. Oceanogr., 33(4), 677-693,

808 https://doi.org/10.1175/1520-0485(2003)33<677:soteui>2.0.co;2, 2003.

809 Hisard, P., and Hénin, C.: Response of the equatorial Atlantic Ocean to the 1983–1984 wind

810 from the Programme Français Océan et Climat dans l'Atlantique Equatorial cruise data set, J.

811 Geophys. Res.-Oceans, 92(C4), 3759-3768, https://doi.org/10.1029/jc092ic04p03759, 1987.

812 Hormann, V., and Brandt, P.: Atlantic Equatorial Undercurrent and associated cold tongue

813 variability, J. Geophys. Res.-Oceans, 112(C6), https://doi.org/10.1029/2006jc003931, 2007.

814 Hormann, V., Lumpkin, R., and Foltz, G. R.: Interannual North Equatorial Countercurrent

815 variability and its relation to tropical Atlantic climate modes, J. Geophys. Res.-Oceans,

816 117(C4), https://doi.org/10.1029/2011jc007697, 2012.

817 Jochum, M., and Malanotte-Rizzoli, P.: On the generation of North Brazil Current rings, J.

818 Mar. Res., 61(2), 147-173, https://doi.org/10.1357/002224003322005050, 2003.

819 Johns, W. E., Lee, T. N., Schott, F. A., Zantopp, R. J., and Evans, R. H.: The North Brazil

820 Current retroflection: Seasonal structure and eddy variability, J. Geophys. Res.-Oceans,

821 95(C12), 22103-22120, https://doi.org/10.1029/jc095ic12p22103, 1990.

822 Johns, W. E., Lee, T. N., Beardsley, R. C., Candela, J., Limeburner, R., and Castro, B.:

823 Annual cycle and variability of the North Brazil Current, J. Phys. Oceanogr., 28(1), 103-128,

824 https://doi.org/10.1175/1520-0485(1998)028<0103:acavot>2.0.co;2, 1998.

825 Lagerloef, G. S., Mitchum, G. T., Lukas, R. B., and Niiler, P. P.: Tropical Pacific near-surface

826 currents estimated from altimeter, wind, and drifter data, J. Geophys. Res.-Oceans, 104(C10),

827 23313-23326, https://doi.org/10.1029/1999jc900197, 1999.

828 Large, W. G., and Pond, S.: Open ocean momentum flux measurements in moderate to strong

829 winds, J. Phys. Oceanogr., 11(3), 324-336, https://doi.org/10.1175/1520-

830 0485(1981)011<0324:oomfmi>2.0.co;2, 1981.

831 NRSC: OSCAT Wind stress and Wind stress curl products, Ocean Sciences Group, Earth and

832 Climate Science Area, Hyderabad, India, 18 pp., 2013.

833 Peterson, R. G., and Stramma, L.: Upper-level circulation in the South Atlantic Ocean, Prog.

834 Oceanogr., 26(1), 1-73, https://doi.org/10.1016/0079-6611(91)90006-8, 1991.

Provost, C., Arnault, S., Chouaib, N., Kartavtseff, A., Bunge, L., and Sultan, E.: TOPEX/Poseidon and Jason equatorial sea surface slope anomaly in the Atlantic in 2002: Comparison with wind and current measurements at 23W, Mar. Geod., 27(1-2), 31-45, https://doi.org/10.1080/01490410490465274, 2004.

Pujol, M. I., Faugère, Y., Taburet, G., Dupuy, S., Pelloquin, C., Ablain, M., and Picot, N.: DUACS DT2014: the new multi-mission altimeter data set reprocessed over 20 years, Ocean Sci., 12(5), 1067-1090, https://doi.org/10.5194/os-2015-110, 2016.

Richardson, P. L., and Walsh, D.: Mapping climatological seasonal variations of surface currents in the tropical Atlantic using ship drifts, J. Geophys. Res.-Oceans, 91(C9), 10537-10550, https://doi.org/10.1029/jc091ic09p10537, 1986.

Rodrigues, R. R., Rothstein, L. M., and Wimbush, M.: Seasonal variability of the South Equatorial Current bifurcation in the Atlantic Ocean: A numerical study, J. Phys. Oceanogr., 37(1), 16-30, https://doi.org/10.1175/jpo2983.1, 2007.

Schmitz Jr, W. J., and McCartney, M. S.: On the north Atlantic circulation, Rev. Geophys., 31(1), 29-49, https://doi.org/10.1029/92RG02583, 1993.

Schott, F. A., Stramma, L., and Fischer, J.: The warm water inflow into the western tropical Atlantic boundary regime, spring 1994, J. Geophys. Res.-Oceans, 100(C12), 24745-24760, https://doi.org/10.1029/95jc02803, 1995.

Schott, F. A., Fischer, J., and Stramma, L.: Transports and pathways of the upper-layer circulation in the western tropical Atlantic, J. Phys. Oceanogr., 28(10), 1904-1928, https://doi.org/10.1175/1520-0485(1998)028<1904:tapotu>2.0.co;2, 1998.

Schott, F. A., McCreary Jr, J. P., and Johnson, G. C.: Shallow overturning circulations of the tropical-subtropical oceans, Washington DC American Geophysical Union Geophys. Monogr. Ser., 147, 261-304, https://doi.org/10.1029/147gm15, 2004.

Servain, J.: Simple climatic indices for the tropical Atlantic Ocean and some applications, J. Geophys. Res.-Oceans, 96 (C8), 15137-15146, https://doi.org/10.1029/91jc01046, 1991.

Silva, M., Araujo, M., Servain, J., Penven, P., and Lentini, C. A.: High-resolution regional ocean dynamics simulation in the southwestern tropical Atlantic. Ocean Model., 30(4), 256-269, https://doi.org/10.1016/j.ocemod.2009.07.002, 2009.

864   Stramma, L., and Schott, F.: The mean flow field of the tropical Atlantic Ocean, Deep-Sea

865   Res. Pt. II, 46(1-2), 279-303, https://doi.org/10.1016/s0967-0645(98)00109-x, 1999.

866   Stramma, L., and England, M.: On the water masses and mean circulation of the South

867   Atlantic Ocean, J. Geophys. Res.-Oceans, 104(C9), 20863-20883,

868   https://doi.org/10.1029/1999JC900139, 1999.

869   Sudre, J., Maes, C., and Garçon, V.: On the global estimates of geostrophic and Ekman

870   surface currents, Limnol. Oceanogr.: Fluids Environ., 3(1), 1-20,

871   https://doi.org/10.1215/21573689-2071927, 2013.

872   Trenberth, K. E., Large, W. G., and Olson, J. G.: The mean annual cycle in global ocean wind

873   stress, J. Phys. Oceanogr., 20(11), 1742-1760, https://doi.org/10.1175/1520-

874   0485(1990)020<1742:TMACIG>2.0.CO;2, 1990.

875   Tuchen, F. P., Lübbecke, J. F., Schmidtko, S., Hummels, R., and Böning, C. W. : The Atlantic

876   subtropical cells inferred from observations, J. Geophys. Res.-Oceans, *124*(11), 7591-7605,

877   https://doi.org/10.1029/2019JC015396, 2019.

878   Tuchen, F. P., Lübbecke, J. F., Brandt, P., and Fu, Y.: Observed transport variability of the

879   Atlantic Subtropical Cells and their connection to tropical sea surface temperature variability.

880   J. Geophys. Res.-Oceans, *125*(12), e2020JC016592, https://doi.org/10.1029/2020JC016592,

881   2020.

882   Tuchen, F.P., Brandt, P., Lübbecke, J. F., and Hummels, R.: Transports and Pathways of the

883   Tropical AMOC Return Flow From Argo Data and Shipboard Velocity Measurements. J.

884   Geophys. Res.-Oceans, 127 (2), e2021JC018115, https://doi.org/10.1029/2021JC018115,

885   2022.

886   Urbano, D. F., Jochum, M., and Da Silveira, I. C. A.: Rediscovering the second core of the

887   Atlantic NECC, Ocean model., 12(1-2), 1-15, https://doi.org/10.1016/j.ocemod.2005.04.003,

888   2006.

889   Urbano, D. F., De Almeida, R. A. F., and Nobre, P.: Equatorial Undercurrent and North

890   Equatorial Countercurrent at 38 W: A new perspective from direct velocity data, J. Geophys.

891   Res.-Oceans, 113(C4), https://doi.org/10.1029/2007jc004215, 2008.

892   Verdy, A., and Jochum, M.: A note on the validity of the Sverdrup balance in the Atlantic

893   North Equatorial Countercurrent, Deep-Sea Res. Pt. I, 52(1), 179-188,

894   https://doi.org/10.1016/j.dsr.2004.05.014, 2005.

895   Zebiak, S. E.: Air–Sea Interaction in the Equatorial Atlantic Region, J. Clim., 6 (8), 1567-

896   1586, https://doi.org/10.1175/1520-0442(1993)006<1567:AIITEA>2.0.CO;2, 1993.

897   Zheng, Y., and Giese, B. S.: Ocean heat transport in simple ocean data assimilation: Structure

898   and mechanisms, J. Geophys. Res.-Oceans, 114(C11), https://doi.org/10.1029/2008jc005190,

899   2009.